

# Noninvasive Photoacoustic and Fluorescence Sentinel Lymph Node Identification using Dye-Loaded Perfluorocarbon Nanoparticles

Walter J. Akers,<sup>†,||</sup> Chulhong Kim,<sup>‡,||</sup> Mikhail Berezin,<sup>†</sup> Kevin Guo,<sup>†</sup> Ralph Fuhrhop,<sup>§</sup> Gregory M. Lanza,<sup>§</sup> Georg M. Fischer,<sup>†</sup> Ewald Daltrozzo,<sup>†</sup> Andreas Zumbusch,<sup>†</sup> Xin Cai,<sup>‡</sup> Lihong V. Wang,<sup>‡,\*</sup> and Samuel Achilefu<sup>†,‡,\*</sup>

<sup>†</sup>Department of Radiology and <sup>‡</sup>Department of Biochemistry & Molecular Biophysics, Washington University School of Medicine, 4525 Scott Avenue, Saint Louis, Missouri 63108, United States, <sup>†</sup>Department of Biomedical Engineering, Washington University, One Brookings Drive, St. Louis, Missouri 63130, United States, <sup>§</sup>C-TRAIN and Division of Cardiology, Washington University School of Medicine, 4320 Forest Park Avenue, St. Louis, Missouri 63108, United States, <sup>†</sup>Fachbereich Chemie, University of Konstanz, 78457 Konstanz, Germany. <sup>||</sup>These authors contributed equally on this work.

The nodal status of cancer is an important prognostic indicator for patients diagnosed with melanoma,<sup>1</sup> gynecological cancers,<sup>2</sup> breast cancer,<sup>3</sup> prostate cancer,<sup>4,5</sup> and other forms of solid cancer. The metastatic spread of cancer cells occurs by the local invasion of adjacent tissue and dissemination in the bloodstream *via* the lymphatic system. Cancer cells that migrate from the primary tumor may become lodged in the first lymph nodes draining the tumor area. From that lymph node, the tumor cells migrate further into other lymph nodes and the bloodstream, leading to a wider spread of the cancer. The closest lymph node that drains the tumor area is called the sentinel lymph node (SLN). The SLN represents the most probable first location of metastatic spread.<sup>3</sup> Identification of the SLN is commonly performed in clinics invasively using a colloid of radionuclide, such as the <sup>99m</sup>Tc-labeled sulfur colloid,<sup>6,7</sup> and/or injection of a dye, such as isosulfan blue or methylene blue,<sup>8,9</sup> subcutaneously in tissue surrounding the tumor location at the time of surgery. After initial clearance of the probe, the nearby tissue is dissected and the location of the SLN is determined by a hand-held scintillator as a hot spot or visually as a blue-stained tissue. The SLN is removed and examined immediately by a pathologist using standard intraoperative histological protocol.<sup>10–12</sup> If cancer cells are detected in the SLN, surgical resection of the secondary lymph nodes (radical resection) is per-

**ABSTRACT** The contrast mechanisms used for photoacoustic tomography (PAT) and fluorescence imaging differ in subtle, but significant, ways. The design of contrast agents for each or both modalities requires an understanding of the spectral characteristics as well as intra- and intermolecular interactions that occur during formulation. We found that fluorescence quenching that occurs in the formulation of near-infrared (NIR) fluorescent dyes in nanoparticles results in enhanced contrast for PAT. The ability of the new PAT method to utilize strongly absorbing chromophores for signal generation allowed us to convert a highly fluorescent dye into an exceptionally high PA contrast material. Spectroscopic characterization of the developed NIR dye-loaded perfluorocarbon-based nanoparticles for combined fluorescence and PA imaging revealed distinct dye-dependent photophysical behavior. We demonstrate that the enhanced contrast allows detection of regional lymph nodes of rats *in vivo* with time-domain optical and photoacoustic imaging methods. The results further show that the use of fluorescence lifetime imaging, which is less dependent on fluorescence intensity, provides a strategic approach to bridge the disparate contrast reporting mechanisms of fluorescence and PA imaging methods.

**KEYWORDS:** cancer · metastasis · prognosis · optical · biopsy · perfluorocarbon

formed to eradicate the tumor or prevent further metastasis. Although these techniques have improved surgical practice and prevented the further spread of cancer, less invasive, highly sensitive, and more accurate localization of SLNs would further improve patient care. Toward these goals, optical and hybrid methods for noninvasive SLN detection have been developed, including fluorescence detection<sup>13,14</sup> and photoacoustic (PA) imaging.<sup>15,16</sup>

Fluorescent optical imaging is a well-known method for *in vivo* imaging, and PA imaging is a recent development that combines optical absorption contrast and fine ultrasonic resolution. The advantage of the lymph node detection using PA imaging has been demonstrated at depths of more

\*Address correspondence to achilefu@mir.wustl.edu (S.A.), lhwang@biomed.wustl.edu (L.V.W.).

Received for review September 3, 2010 and accepted December 07, 2010.

Published online December 20, 2010. 10.1021/nn102274q

© 2011 American Chemical Society

than 30 mm with a resolution of 0.5 mm.<sup>15</sup> Both fluorescence and PA imaging modalities utilize nonionizing radiation and are, therefore, safer to patients and medical staff relative to nuclear imaging methods.

To improve detection sensitivity, both fluorescence and PAT methods require contrast reagents with high absorption coefficients in the NIR spectral region. Unfortunately, commonly used blue dyes for SLN imaging absorb light below 700 nm, minimizing the assessment of deep tissue because endogenous chromophores will rapidly attenuate the light penetration depth. In the first clinical trial, indocyanine green (ICG), a NIR fluorescent dye emitting at ~800 nm, has been successfully evaluated as a new method for SLN biopsy in breast cancer patients. The method facilitated noninvasive visualization of lymphatic vessels and nodes as well as intraoperative identification of the SLN.<sup>17</sup> In contrast to fluorescence methods that require probes with high fluorescence quantum efficiency, the probes for PAT should be minimally emissive, enhancing conversion of absorbed light energy to heat and subsequently to an acoustic signal. Correspondingly, a combined modality requires a probe with a moderate fluorescence quantum yield to generate both an emission and a PA signal simultaneously. To accomplish these goals, we explored the potential of starting with dyes with high and low fluorescence yields. However, lymphatic vessels are permeable, allowing the diffusion of small molecules back into the tissue. Retaining molecular probes exclusively in the lymphatic vessels, therefore, requires their conjugation to macromolecules or formulation in nanoparticles. In addition to minimizing the spread of imaging probes beyond the SLN area, minimum retention of the probe at the site of injection is essential for accurate localization of the SLN.<sup>18</sup> The currently used radioactive <sup>99m</sup>Tc-labeled sulfur colloid tends to remain at the site of administration, slowly diffusing to a lymph node and, therefore, producing a weak signal at the SLN.<sup>19</sup> Because of their small molecular size, blue dyes quickly pass to secondary nodes, leading to difficulties in distinguishing the SLN from other nodes. It has been demonstrated that the solution to the problem lies in the application of hydrophilic nanoparticles, such as <sup>99m</sup>Tc-labeled liposomes with encapsulated dyes<sup>20</sup> and other nanoparticles,<sup>18</sup> which can rapidly move through the lymphatic system to the SLN and are retained there for a period long enough for surgery to be performed.

Herein, we investigated new perfluorocarbon (PFC) nanoparticles loaded with NIR dyes as potential contrast reagents for SLN mapping in rats using PA and fluorescence contrast *in vivo* (Figure 1). We previously demonstrated that receptor targeted PFC nanoparticles have great potential for biomedical imaging and drug delivery applications<sup>21,22</sup> and can be utilized for fluorescence imaging.<sup>23</sup> Two different NIR fluorescent probes with disparate fluorescence efficiencies were used in the new PFC-based nanoparticle formulations

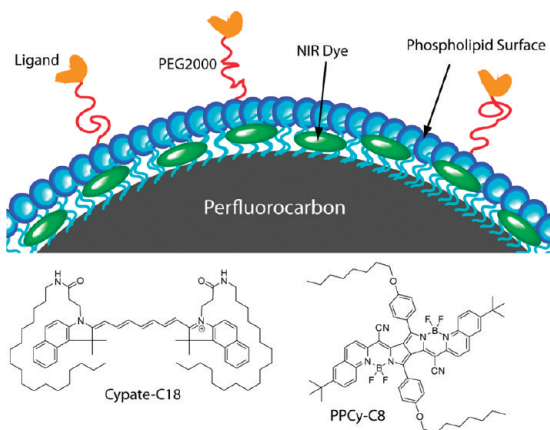


Figure 1. Structure of NIR fluorescent dyes cypate-C18 and pyrrolopyrrole cyanine (PPCy-C8) and schematic of dye-loaded PFC nanoparticles. The perfluorocarbon core is encapsulated in an amphiphilic phospholipid layer (blue) containing hydrophobic dyes (green).

to provide fluorescence and PA contrast (Figure 1). Our results demonstrate the efficacy of lymph node mapping with both modalities. More importantly, formulation of the NIR dye with high fluorescence efficiency resulted in a high PA signal due to the intermolecular fluorescence quenching effect.

## RESULTS AND DISCUSSION

The detection of lymph nodes *in vivo* was previously demonstrated using the NIR fluorescent agent, ICG,<sup>24</sup> but very high concentrations of the dye were needed. We hypothesized that incorporation of NIR dyes in the PFC nanoparticles would improve PA contrast at a relatively smaller dye content. We explored PFC-based nanoparticles incorporating two different NIR fluorescent dyes, PPCy-C8 and cypate-C18, as PA and fluorescence imaging agents in this study. The contrast agents were first analyzed *in vitro* by fluorescence lifetime (FLT) and PA measurements of dyes and nanoparticles in solution. This characterization was followed by *in vivo* time-domain diffuse optical imaging and a hand-held PAT system to demonstrate potential applications of these novel contrast agents in biomedical imaging.

Although a variety of biocompatible emulsion-based nanoparticle systems have been developed for optical imaging,<sup>25,26</sup> PFC-based nanoparticles are viable materials for noninvasive detection. PFC is a biocompatible component that has a 3-day half-life in the body and is completely eliminated through expired air *via* the lungs.<sup>21</sup> We have developed methods for decorating the surface of PFC nanoparticles with contrast and targeting agents by noncovalent mechanisms, eliminating complex and low-yield synthetic steps.<sup>27</sup> Thus, we developed NIR fluorescent PFC nanoparticles for optical and PA imaging by incorporating NIR hydrophobic dyes, cypate-C18<sup>23</sup> and PPCy-C8<sup>28</sup> (C18 and C8 indicate the number of carbons in a hydrophobic chain), in the surface layer.

TABLE 1. Optical Properties of Cypate-C18 and PPCy-C8 Free in Solution and Incorporated in PFC-Based Nanoparticles<sup>a</sup>

probes	solvent	$\lambda$ , abs	$\lambda$ , em	$\epsilon$ , $M^{-1} cm^{-1}$	$\Phi$	$\tau$ , ns	soluble in water	ref
cypate-C18	DMSO	790	815	242 000	0.09	0.83	no	23
PPCy-C8	chloroform	754	766	205 000	0.59	4.36	no	28
cypate-C18/PFC	water	797	813	283 000	0.04	n/m	yes	23
PPCy-C8/PFC	water	789	n/f	50 000	n/f	n/f	yes	23

<sup>a</sup>Abbreviations:  $\epsilon$ , molar absorptivity;  $\Phi$ , quantum yield;  $\tau$ , FLT; n/f, nonfluorescent; n/m, not measured; DMSO, dimethylsulfoxide.

**Spectroscopy.** We explored the use of two NIR fluorescent dyes, PPCy-C8 and cypate-C18, as PA and fluorescence imaging agents in this study. The synthesis and optical properties of these dyes (absorption, emission, and FLT) were reported previously.<sup>23,28,29</sup> Both dyes possess high molar absorptivity in the NIR range,  $>200\ 000\ M^{-1} cm^{-1}$ . Cypate-C18 has a moderate fluorescence quantum yield and a relatively short FLT due to the flexible excited-state structure.<sup>23,30</sup> In contrast, PPCy-C8 with its highly rigid skeleton ensured by complexation with disubstituted boron possesses a high fluorescence quantum yield and a much longer FLT (Table 1). Both dyes have long hydrophobic tails for stable insertion into the phospholipid layer on the surface of the nanoparticles. The dyes were successfully loaded in PFC nanoparticles using a standard protocol (see Methods). All nanoparticles were uniformly distributed with a  $220 \pm 11\ nm$  mean diameter and less than 10% polydispersity as determined by DLS. Upon incorporation in the phospholipid shell, cypate-C18 retained the NIR absorption and emission properties of the base molecule in 0.1–0.3 mol %. The detailed optical characterization of the cypate-C18/PFC-nanoparticle was reported previously.<sup>23</sup>

In contrast to cypate-C18, the PPCy-C8 fluorescence properties were altered upon incorporation in nanoparticles. The absorption spectrum of the incorporated dye showed a significant bathochromic shift from 754 nm in chloroform to 789 nm in the PFC nanoparticle system in water (Table 1 and Figure 2A). The shift was accompanied by a substantial decrease in molar absorptivity and fluorescence yield. Highly emissive properties of the PPCy-C8 dye completely disappeared, and

the emission spectrum of the PPCy-C8/PFC nanoparticles in water was very similar to the emission spectrum of the control PFC nanoparticles with no dye (Figure 2B). The optical properties of the pure dyes cypate-C18 and PPCy-C8 were determined in organic solvents because they are not soluble in water.

The drastic alteration in optical properties of PPCy-C8/PFC nanoparticles could be attributed to a variety of factors, including chemical instability of the dye upon formulation. To demonstrate stable incorporation, the dye was extracted with DCM and the optical properties of the extract were recorded. Absorption and emission properties of the extract were identical to that of the original dye (Supporting Information, Figure S1), clearly demonstrating the structural integrity of the dye.

To further understand the underlying mechanism of changes in the optical properties, we investigated the behavior of the dye in different solvents. The change in polarity from chloroform to methanol caused a hypsochromic shift (Figure 3) while retaining strong fluorescence. Thus, solvent polarity alone is not a compelling reason for spectral change. However, we observed an alteration of the absorption spectra of PPCy-C8 in methanol over time from a spectrum similar to PPCy-C8 in DCM to that of PPCy-C8/PFC in water (Figure S2, Supporting Information). This transformation suggests aggregation of the hydrophobic dye in a polar environment. Similar changes in the absorption spectra with characteristic peaks at  $\sim 790$  and  $\sim 710\ nm$  were also observed upon addition of water to a methanol solution of the dye (Figure S3A,B, Supporting Information), resulting in similar optical properties (Figure S3C, Supporting Information) and indicating similar

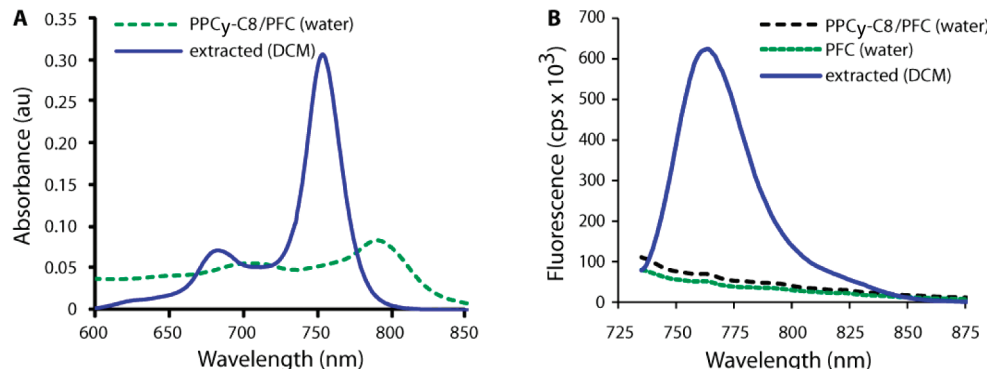


Figure 2. Absorption (A) and emission (B) of PPCy-C8/PFC nanoparticles in water and after extraction of the dye from liposome with dichloromethane (DCM). Ex. = 720 nm. Absorption spectrum of PPCy-C8/PFC was corrected by the absorption of PFC with no dye.

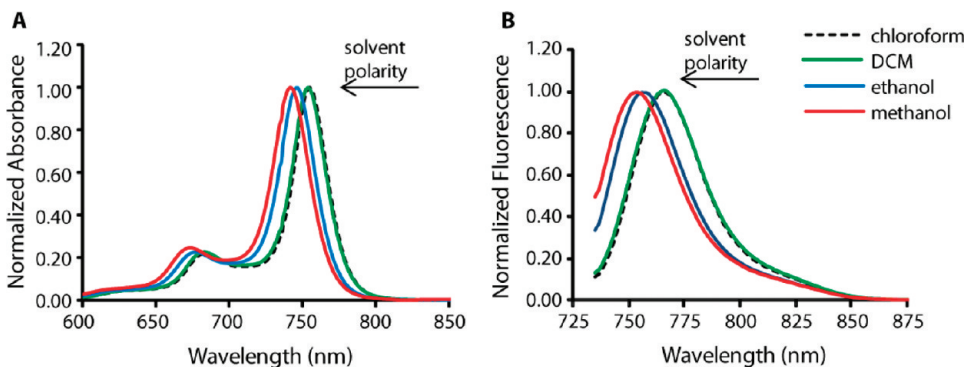


Figure 3. Shift in absorption (A) and emission (B) of PPCy-C8 in different solvents (concn = 1.3  $\mu$ M in all solutions, ex. = 720 nm).

mechanisms of interaction in both solvent systems. Alterations of the absorption spectra were accompanied by strong fluorescence quenching (Figure S3B, Supporting Information). On the basis of these results, we postulate that the change in absorption spectra and fluorescence quenching of the dye incorporated in PFC nanoparticles were due to dye aggregation promoted by the presence of water.

Addition of water (within the range of 5–10 vol %) on the time-scale of seconds gives time-dependent changes that are ascribed to diffusion processes. Clear isosbestic points (Figure S2, Supporting Information) are good indicators that neither significant precipitation nor a variety of differently large aggregates occurred. The observed effects can be explained with the formation of dimers rather than higher aggregates with the monomeric units shifted longitudinally and with an angle of about 30–60° between the long axes, representing the direction of the transition moment of the first electronic transition. These interpretations are supported by the observed isosbestic points in the absorption spectra and the occurrence of a short wavelength band in addition to the long wavelength band, as shown by the splitting of the 740 nm band into bands at 796 and 703 nm, respectively (Figure 2). Because of a relatively flat twisting (torsional) potential, a significant variation of the angle between the monomer transition moments is expected at room temperature. Thus, around the thermodynamically most preferred angle, a dynamic equilibrium of conformations with larger or smaller angles produces an increase of the band half-widths under dimerization. This mobility (low torsional rigidity) in the first excited electronic state should be an efficient channel for the radiationless deactivation, resulting in loss of radiative transfer fluorescence.

The increased loading of the dyes on PFC from 0.1% to 0.3% did not affect optical properties of particles. Absorption properties of PPCy-C8/PFC were proportional to the loading change, making the nanoparticles greener in hue, with no increase in fluorescence observed. Optical properties of the PPCy-C8/PFC helped to elucidate the structural features of the nanoparticles.

Specifically, the data suggest that the PPCy-C8 molecules in PPCy-C8/PFC nanoconstruct are exposed to the solvent and, therefore, lie outside the shell. The nanoconstruct is stable because the addition of bovine serum albumin solution to the nanoparticle solutions did not change the absorption and emission spectra. Addition of albumin helps to identify if the dye is stably incorporated into a nanoparticle. Hydrophobic dyes bind noncovalently to hydrophobic pockets of albumin, and the binding effect can be detected by a change in fluorescence intensity. Because no change in fluorescence intensity was observed after the addition of albumin, the result unequivocally demonstrated that the dye is stably incorporated within the PFC nanoparticles.

Upon loading in PFC nanoparticles, the dyes behaved differently with respect to the quantum yield of fluorescence and FLT. We hypothesized that the lower fluorescence quantum yield of dyes within the PFC nanoparticles would improve the PA contrast due to the higher heat yield, which, in turn, would generate a stronger ultrasound signal (thermal expansion).<sup>16</sup> Non-quenched nanoparticles are expected to produce a higher fluorescence intensity, but a poor PA signal. Enhanced fluorescence quenching was realized with PPCy-C8 upon formulation in PFC nanoparticles, which retained a relatively high absorption coefficient of the dye ( $\sim 50\,000\,M^{-1}\,cm^{-1}$ ; see Table 1).

PA signals for free dyes and dye-loaded PFC nanoparticles were measured in solution using a noncontact PA microscopy system.<sup>15</sup> We confirmed that no PA signal (comparable to the signal from the background) was observed from PFC nanoparticles without loading any NIR dye (Figure 4). PPCy-C8/PFC nanoparticles produced an  $\sim 3.5$  times greater PA amplitude than a comparable concentration (0.3 mol %) of cypate-C18/PFC and a significantly higher signal ( $\sim 9$  times) than whole blood (Figure 4). We found that the free dyes did not produce a sufficient PA signal *in vitro* for further applications at equivalent dye concentrations for *in vivo* study (data not shown).

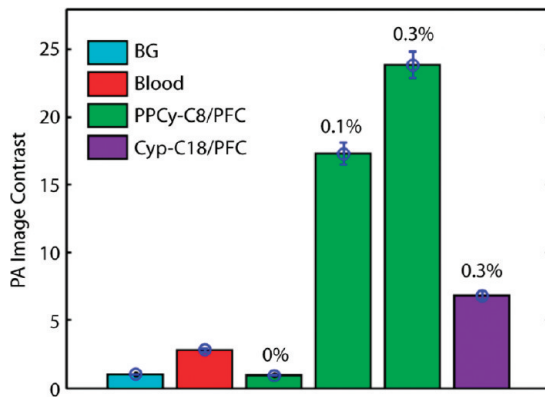


**Figure 4.** Comparison of PPCy-C8/PFC and cypate-C18/PFC nanoparticle PA image contrasts relative to whole blood at an optical wavelength of 767 nm. The concentration of PPCy-C8 varied from 0.1 to 0.3 mol %. BG = background.

Fluorescence quenching of PPCy-C8 in the PFC nanoparticles could be attributed to exposure to an aqueous medium or self-aggregation. Either way, the net result is the conversion of absorbed light to heat, which improved the PA contrast through tissue thermal expansion. The high PA signal of PPCy-C8/PFC nanoparticles relative to equivalent concentrations of cypate-C18/PFC (Figure 4) is likely due to the difference in fluorescence properties of the dyes after formulation rather than before. This assumption is corroborated by the intense quenching present in the PPCy-C8/PFC nanoparticles, as evidenced by the lower fluorescence yield and very short FLT. The cypate-C18/PFC nanoparticles are approximately 3 times higher in fluorescence yield relative to PPCy-C8/PFC, in contrast to the yield of the free dyes.

**In Vivo Imaging.** Before the injection of nanoparticles, the measured autofluorescence intensity in the lymph node region was low and FLTs could not be calculated (Figure S5, Supporting Information). After injection of PFC-based nanoparticles subcutaneously in the forepaw of rats, fluorescence from the lymph nodes was distinct at 1 and 24 h after injection (Figure 7). Data comparison shows that the measured fluorescence intensity for the lymph node region was not higher than 4 cps (normalized by laser power and integration time) for the preinjection scans, approximately 200 cps for PPCy-C8/PFC nanoparticles, and greater than 600 cps for cypate-C18/PFC. The significant ( $P > 0.01$ ) increase in fluorescence for cypate-C18/PFC compared with PPCy-C8/PFC particles was a direct consequence of highly quenched PPCy-C8 dye and possible exposure to water.

PAT was performed using the same rat model described above after subcutaneous injection of contrast agent solutions in the front paws. Lymph nodes were detected by PAT at 3 h after injection, with excellent contrast at 24 h after injection (Figure 5A–C). The cor-

responding B-scan images of lymph nodes clearly show the depth position of each lymph node (Figure 5A1–C1). The average PA image contrasts of SLNs ( $n = 3$  rats) at 3 and 24 h postinjection are  $8.7 \pm 1.3$  and  $12.3 \pm 3.4$ , respectively (Figure 5D). On the basis of *in vivo* spectroscopic PA analysis, which follows the trend of the *in vitro* PA spectrum, we confirmed that the measured PA amplitudes *in vivo* stemmed from lymph nodes containing PPCy-C8/PFC nanoparticles (Figure 5E).

After imaging, the animals were euthanized and lymph nodes removed. PA and fluorescence imaging were performed *ex vivo* to confirm the location of the signal to the lymph node tissue and to assess the signal levels obtained *in vivo* relative to direct detection. The axillary lymph node chain was detected *in vivo* and confirmed by *ex vivo* imaging (Figure 6A). Obvious fluorescence and PA signals were observed from three excised lymph nodes from the left lymph node region (injection site), whereas both signals were too weak in one dissected lymph node from the right region (no injection site). The PA image contrasts quantified from *in vivo* and *ex vivo* PA imaging results agreed well, and the *ex vivo* fluores-

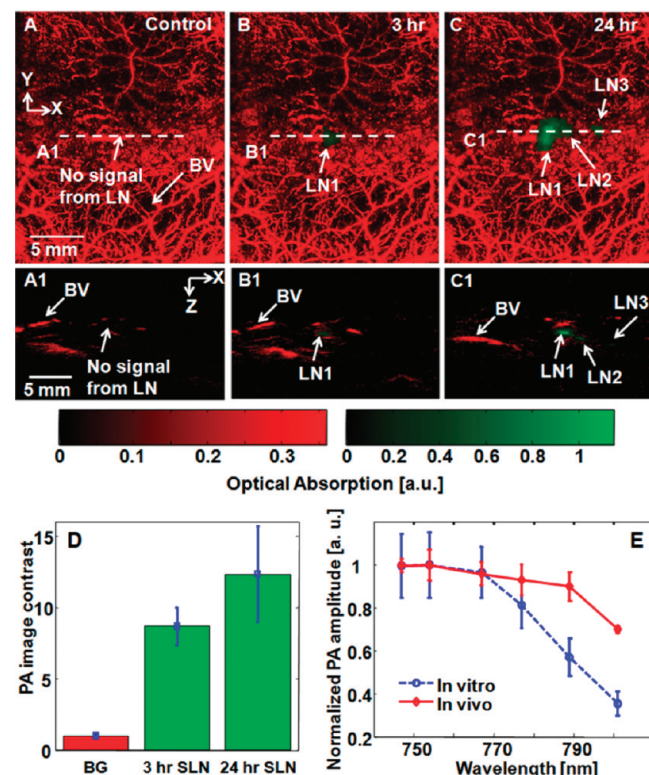


**Figure 5.** Noninvasive PA MAP images of the left axillary region of a rat. (A) Control image acquired before PPCy-C8/PFC nanoparticles. (B) PA image at 3 h postinjection. (C) PA image at 24 h postinjection. (A1–C1) Corresponding B-scan images along the cuts A1–C1, in (A–C). (D) Average PA image contrast from SLNs at 3 and 24 h postinjection ( $n = 3$ ). Error bars represent SD. (E) Comparison of spectroscopic PA amplitudes between *in vitro* and *in vivo* results. Abbreviations/color code: BV, blood vessels; LN, lymph node; SLN, sentinel lymph node; BG, background; red color, blood vessels; green color, lymph nodes.

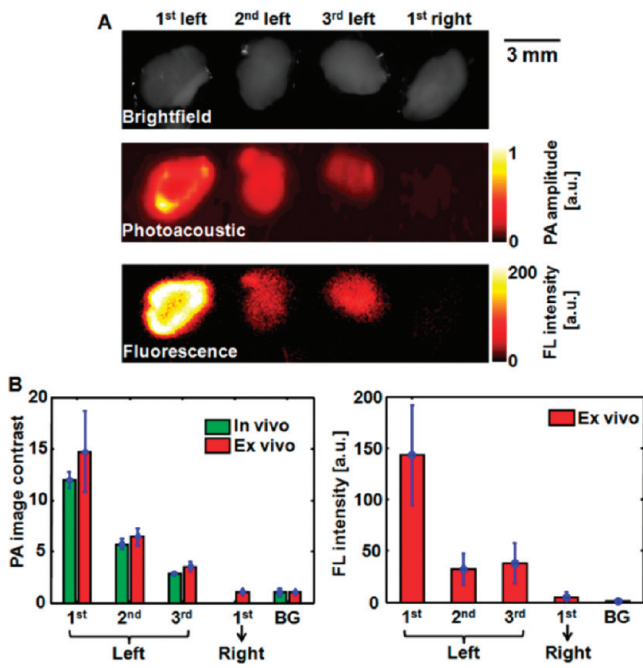


Figure 6. (A) Bright-field, PA, and FL images of ex vivo lymph nodes 24 h after intradermal administration of PPCy-C8/PFC nanoparticles into the left forepaw of the rat. (B) Comparison of PA image contrasts quantified from *in vivo* and *ex vivo* results, and fluorescence intensity from *ex vivo* results. Abbreviations: PA, photoacoustic; FL, fluorescence; BG, background.

cence imaging results confirmed this finding (Figure 6B), demonstrating the feasibility of using these nanoparticles for PA and fluorescence mapping of lymph nodes.

Fluorescence imaging was also performed for detecting lymph nodes in the same animal model. The fluorescence intensity and FLT maps for free dyes and dye-loaded PFC nanoparticles are shown in Figure 7. The cypate and PPCy-C8 were transported to the regional lymph nodes faster than the nanoparticles and were imaged at 1 and 4 h postinjection. FLT measurements shown in Figure 7 and obtained from decay curves (Figure 8) demonstrated the quenched state of the PPCy-C8/PFC relative to cypate-C18/PFC nanoparticles. The FLT of free PPCy-C8 in the lymph node was greater than 3 ns, whereas the PPCy-C8/PFC nanoparticles showed only 0.22 ns, close to the lowest minimum resolution of the imager. The fluorescence intensity from the PPCy-C8 nanoparticles was also very low relative to that of the free dye. In contrast, the mean FLT of cypate-C18/PFC was very close to that of the free dye.

The FLT was measured by single-exponential fitting of the fluorescence decay curves acquired as temporal point spread functions by the time-correlated single-photon counting (TCSPC) detector. Representative decay curves and fitted lifetimes are shown in Figure 8.

Both optical reporter systems provided contrast for fluorescence and PA detection, although the PPCy-C8/

PFC nanoparticles demonstrated enhanced PA contrast. A possible alternative explanation of the drastic differences in the PA properties of the two dye–nanoparticle formulations is based on the orientation of the dyes within the material. In the case of C18/PFC nanoparticles, both the fluorescence quantum yield and lifetime measurements indicate that the dyes were sequestered inside the hydrophobic core of the nanoparticle formulation. This suggests that local heat generated by the system could be absorbed by the phospholipid outer layer, thereby attenuating the resultant PA signal. In contrast, the dye in the PPCy-C8/PFC formulation is possibly exposed to the outer aqueous phase, which results in direct deposition of heat to the immediate surrounding and detectable as the PA signal. The concerted effect of many dye molecules per nanoparticles will further enhance the net PA signal. This reasoning provides a strategy for optimizing the dye formulation for either PA or fluorescence contrast.

Interestingly, the PPCy-C8/PFC FLT remained low for the duration of the *in vivo* study, indicating that leakage of the dye from the nanoparticles did not occur in detectable amounts. It is possible that the dye was released, but remained in a quenched state due to aggregation, though from previous reports, we would expect the lifetime to report on diffusion of the hydrophobic dye.<sup>31</sup>

Relative to the small molecule fluorophores, the C18/PFC nanoparticles provided higher SLN contrast due to more significant accumulation in the first lymph node. The small molecule agents traveled faster to the SLN, progressing to second and third lymph nodes, and draining into the circulatory system. *Ex vivo* fluorescence imaging of lymph nodes showed differences in diffusion patterns between free dyes and nanoparticles. The free dyes appear to have diffused along the lymph node chain, with fluorescence from cypate-C18 nearly equally distributed among the three lymph nodes. PPCy-C8 fluorescence was higher in the second and third lymph nodes than in the first, which corresponds to the *in vivo* imaging results in Figure 6. The nanoparticles showed a more progressive diffusion pattern along the chain, with the first lymph node having a significantly higher fluorescence intensity than the following two nodes ( $P < 0.05$ ). Interestingly, the fluorescence intensity from the first lymph nodes was generally higher for the nanoparticles than for the free dyes. These differences are likely due to the faster transport of the free dyes through the lymph nodes relative to the nanoparticles. Previous studies have shown that fast migration is not a benefit in SLN detection, but rather, high accumulation in the LN of interest is more important.<sup>30</sup> Thus, these PFC nanoparticles are excellent contrast agents for noninvasive SLN detection and subsequent biopsy or resection.

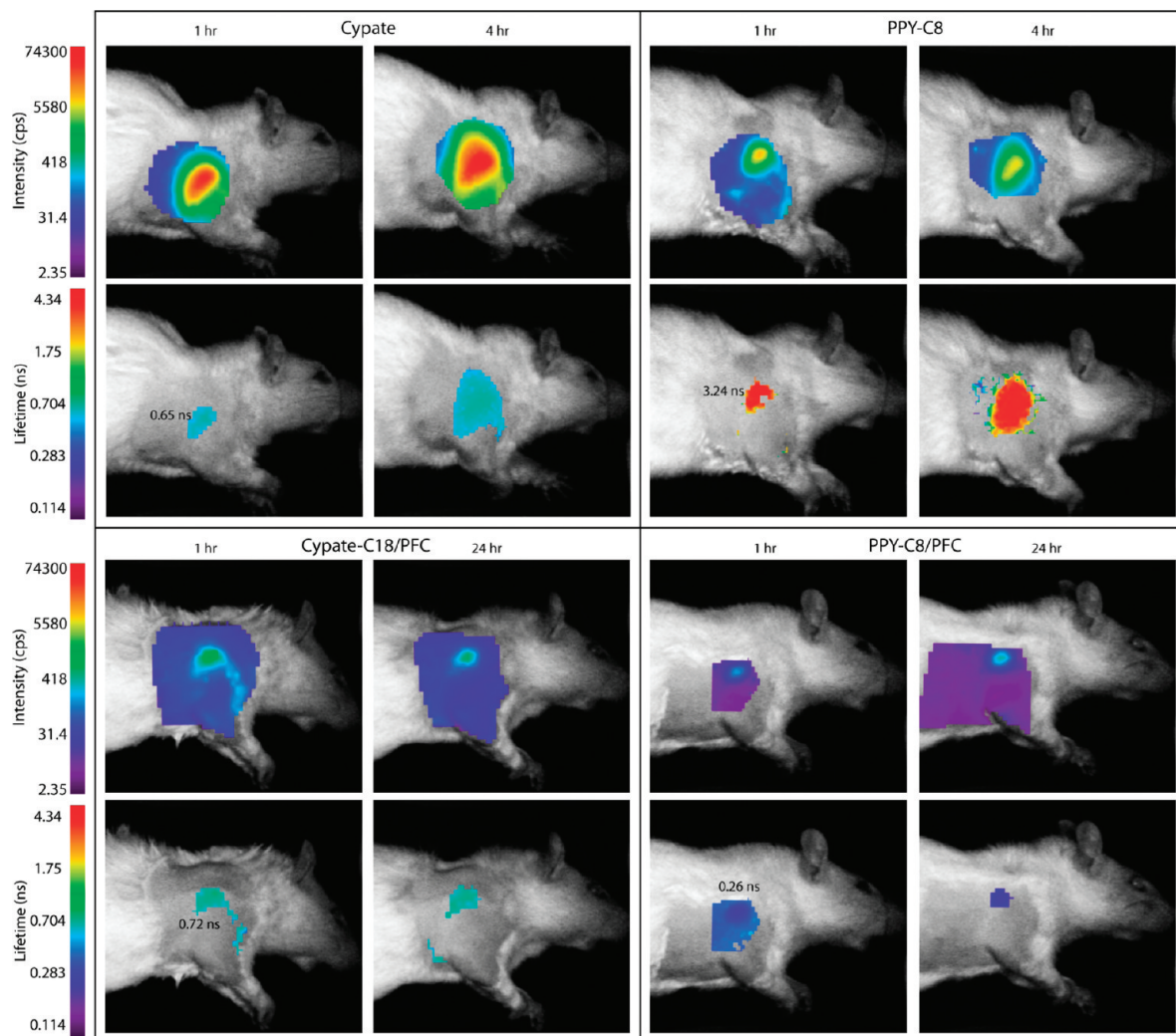


**Figure 7.** Fluorescence intensity and lifetime maps of rats at indicated times after subcutaneous injection of contrast agents in the forepaw. The intensity maps indicate the relative concentration of contrast agents within the axillary area at given times, whereas the FLT maps show the differences in contrast agents used. The FLTs of cypate and cypate-C18/PFC nanoparticles are almost equal, whereas the free PPCy-C8 has a much higher FLT relative to that of the PPCy-C8/PFC nanoparticles.

### CONCLUSION

We have demonstrated contrast agents for identification of SLNs by both PA and fluorescence detection systems. Despite similar behavior of fluorescent dyes, loading of these dyes in PFC nanoparticles resulted in differential contrast for both optical and PA imaging. Enhancement of the PA signal by PPCy-C8/PFC nanoparticles resulted from fluorescence quenching and possible exposure of the dye to an aqueous environment. Because there are multiple dye molecules per nanoparticle, this feature is expected to increase thermal expansion of the immediate environment, leading to a greater acoustic signal. These results also show the benefit of nanomaterials for enhancement of contrast by increased payload per particle. Although we have shown the advantage of a nonfluorescent system for PA imaging, this does not preclude agents for simultaneous detection by both systems. The fluorescence yield reduces PA contrast but does not abolish it. Development of fluorescent and PA contrast agents must

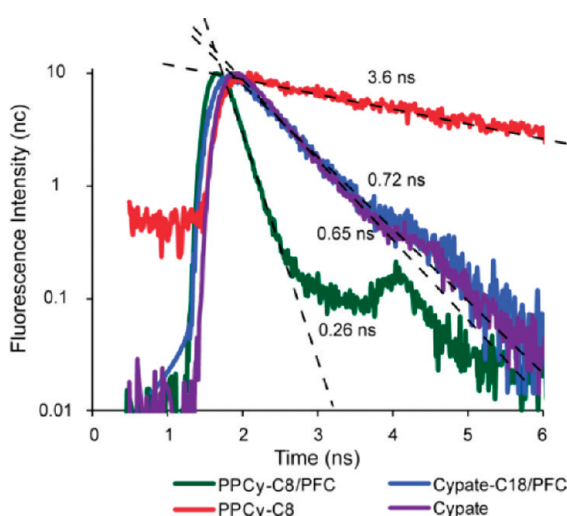


**Figure 8.** Normalized fluorescence decay curves with linear regression lines and calculated FLTs of free dyes and NIR fluorescent nanoparticles in the axillary lymph nodes measured by TD-DOL in living rats.

take into account both absorption and fluorescence yield in the nanoparticle design. It is feasible to use PA for localization at early time points when the dyes are in a quenched state, and fluorescence detection may be used to monitor longitudinally as the PA contrast decreases. The different mechanisms of detection show

the strengths and weaknesses of PA and fluorescence imaging and the advantage of combining the two modalities for noninvasive SLN mapping in cancer diagnosis. Lymph nodes were detected by diffuse optical imaging and PA imaging, showing the capabilities for noninvasive lymph node mapping.

## METHODS

**Materials.** All reagents were spectroscopy grade or synthesized and purified to 95% or greater. DMSO, chloroform, DCM, ethanol, and methanol (spectroscopy grade) were purchased from Sigma-Aldrich (St. Louis, MO). The UV-vis absorption spectra of NPs were collected at room temperature using a Beckman 640 UV-visible spectrophotometer and a quartz cuvette with 10 mm of light path. The fluorescence spectra of NPs were obtained at room temperature using a Fluorolog III fluorescence spectrophotometer (Horiba). FLT was measured using the TC-SPS method, as described previously. The FLTs were determined using an excitation source NanoLED at 700 nm and a monitored emission at 775 nm with a band pass of 20 nm. In all measurements, a three-exponential decay analysis was applied.

**Synthesis.** A hydrophobic derivative of cypate,<sup>32</sup> cypate-C18,<sup>23</sup> and pyrrolopyrrole cyanine, PPCy-C8,<sup>33</sup> were synthesized as previously described. PFC nanoparticles with both hydrophobic dyes were formulated as previously described<sup>23</sup> with the addition of NIR fluorescent dyes for optical and PA imaging. Briefly, the nanoparticles were composed of 20% (v/v) perfluoroctylbromide (PFOB), 2.0% (w/v) of a surfactant comixture, and 1.7% (w/v) glycerin in distilled, deionized water. The surfactant comixture of nanoparticles included 98 mol % lecithin (Avanti Polar Lipids, Inc., Alabaster, AL, U.S.A.), 0.1 mol % peptidomimetic  $\alpha_1\beta_3$ -integrin antagonist conjugated to PEG<sub>2000</sub>-phosphatidylethanolamine (Kereos, Inc., St. Louis, MO, U.S.A.), and 1.9 mol % phosphatidylethanolamine (Avanti Polar Lipids, Inc., Alabaster, AL, U.S.A.). NIR dyes were substituted for lecithin on an equimolar basis from 0.1 to 0.3 mol %. The surfactant components were combined with the PFOB, water, and glycerin; the pH was adjusted to 7.5; and the mixture was emulsified (Microfluidics, Newton, MA, U.S.A.) at 20 000 psi for 4 min. Nominal particle sizes and polydispersity ( $220 \pm 11$  nm with a polydispersity of 0.09) were measured by dynamic light scattering (DLS, Brookhaven Instrument Corp., Holtsville, NY, U.S.A.).

**Spectroscopy.** The spectral properties of these formulations were characterized relative to control nanoparticles without dye. The absorption and emission spectra of dye-loaded PFC nanoparticles were subtracted from absorption and emission of control nanoparticles. Solutions of free dye were formulated by dissolving dye in 20% DMSO in water at a concentration of 40  $\mu$ M. NIR fluorescent nanoparticles were aliquoted (100  $\mu$ L) into 1 mL of PBS in a plastic cuvette and analyzed by absorption and fluorescence.

A stock solution of PPCy-C8 was prepared in DCM (26 mM). An aliquot of 10  $\mu$ L was diluted 200 times with chloroform, DCM, ethanol, and methanol in a quartz cuvette, and the spectra (absorption, fluorescence) were recorded. The FLT of the solutions was measured using a NanoLED 700 nm (Horiba) for excitation and a 775 nm filter for emission. For the aggregation study, 70  $\mu$ L of 0.5 mM of PPCy-C8 in DCM was added to a quartz cuvette filled with 1930  $\mu$ L of methanol for a total concentration of 17  $\mu$ M. The dye concentration and absorption coefficients within PFC nanoparticles were determined by absorption spectroscopy for the nanoparticles and after extraction with DMSO or DCM. The fluorescence quantum yield of the nanoparticles was determined with reference to ICG, which has a quantum yield of 0.01 in water.<sup>30</sup>

**In Vitro Photoacoustic Imaging.** For measurement of the PA signal from nanoparticles, Tygon tubes were filled with aqueous suspensions of PPCy-C8 nanoparticles, cypate-C18 PFC NPs, or dye-free nanoparticles and one tube was filled with whole blood. The sealed tubes were embedded in a water bath. The PA ampli-

tude from the nanoparticle solutions was measured and compared with that from the blood for a PA contrast at 767 nm excitation using a PA imaging system and the method as previously described.<sup>34</sup>

**Animal Models.** All animal studies were approved by the animal studies committee at Washington University School of Medicine. Sprague-Dawley rats (Harlan, Indianapolis, IN) were anesthetized with ketamine and xylazine cocktail (87 mg/kg and 13 mg/kg, respectively, IP). Hair over the axillary region was removed by gentle clipping and depilatory cream. Contrast agent solutions (0.05 mL) were injected subcutaneously in the forepaw prior to imaging. For fluorescence imaging, rats were injected on both sides, whereas for PAT, rats were injected in the left forepaw only. Imaging was performed immediately after injection up to 4 h after injection and again at 24 h after injection.

**In Vivo Fluorescence Imaging.** Fluorescence imaging was performed with the eXplore Optix time-domain diffuse optical imaging system (ART, Montreal, Canada). Animals were placed on the heated imaging platform and adjusted for optimal height. Preinjection scans ( $n = 2$ ) were acquired of the axillary region with a laser power of 500  $\mu$ W and an integration time of 0.3 s. Postinjection scans were acquired at 1 and 4 h after injection for free dyes and 1 and 24 h after injection for nanoparticles. Absorption and emission scans were performed sequentially for all acquisitions. The integration time was kept at 0.3 s per step while the laser power was adjusted to achieve an adequate signal strength for FLT measurement. The step size was 1–3 mm per step. Fluorescence intensity and lifetime maps were constructed from acquired data by integration or curve fitting of the fluorescence temporal point spread function (TPSF), respectively, using Optiview software (ART, Montreal, Canada) as previously described.<sup>31</sup> Fluorescence intensity values are reported in counts per second and were normalized to the laser power and integration time. Mean fluorescence intensity and FLT values were determined by ROI analysis.

**In Vivo Photoacoustic Imaging.** After promising *in vitro* contrast with PPCy-C8-loaded nanoparticles, *in vivo* PA imaging was performed. The three-dimensional PA imaging system is detailed in a previous publication.<sup>15</sup> A light wavelength of 767 nm was used for most of the experiments, but optical wavelengths were tuned from 747 to 801 nm for spectroscopic analysis. For imaging surrounding blood vessels, an optical wavelength of 570 nm was used. The light fluence on the skin was 4 mJ/cm<sup>2</sup>, within the current ANSI limit. A single-element 5 MHz (for sentinel lymph node imaging, V308, Panametrics-NDT) or 50 MHz (for surrounding vasculature imaging, V214-BB-RM, Panametrics-NDT) ultrasound transducer was used as an ultrasonic detector. Axial spatial resolutions of the 5 and 50 MHz PA imaging systems are 144 and 15  $\mu$ m, and lateral resolutions are 560 and 45  $\mu$ m, respectively. The time of arrival of PA waves provides one-dimensional depth-sensitive images (A-line). Mechanical raster scanning in two lateral directions enables forming depth-resolved cross-sectional images (B-scans) and three-dimensional images. Volumetric images were expressed via maximum amplitude projection (MAP), which projected the maximum signal along each A-line onto the corresponding two-dimensional plane. The imaging acquisition time for a 25 mm  $\times$  30 mm field of view was about 25 min. PPCy-C8 nanoparticle solutions (0.5 mg) were administered by injection in the footpads of rats as described above. A series of PA images were acquired to 3 h postinjection, and we obtained another PA image at 24 h postinjection. The differential images of the SLNs before and after injection (*i.e.*, images after injection minus images before injection) were overlaid on the images of blood vessels.

Animals were euthanized after final imaging time points at 24 h (nanoparticles) and 4 h (small molecules) after injection. *Ex vivo* fluorescence imaging of lymph nodes was performed with the Kodak IS4000MM planar reflectance imaging system (Carestream Health, New Haven, CT) with 755 nm excitation and 830 nm emission detection. *Ex vivo* PAT was performed by embedding dissected lymph nodes in the gelatin phantom and imaging. For comparison of fluorescence and PAT contrast, gelatin-embedded lymph nodes were also imaged with a planar reflectance imaging system.

**Acknowledgment.** These studies were funded, in part, by grants from the NIH (R01 EB008111 and R01 EB008458 to S.A. and R01 EB000712, R01 EB008085, R01 CA134539, U54 CA136398, R01 EB010049, and 5P60 DK02057933 to L.V.W.). L.V.W. has a financial interest in Microphotoacoustics, Inc. and in Endra, Inc., which, however, did not support this work.

**Supporting Information Available:** Figures depicting spectroscopic analysis of PPCy-C8 free dye and after extraction from PFC-based nanoparticles, absorption spectra of PPCy-C8 in methanol over time, and absorption spectra of PPCy-C8 in methanol–water solutions. This material is available free of charge via the Internet at <http://pubs.acs.org>.

## REFERENCES AND NOTES

- Phan, G. Q.; Messina, J. L.; Sondak, V. K.; Zager, J. S. Sentinel Lymph Node Biopsy for Melanoma: Indications and Rationale. *Cancer Control* **2009**, *16*, 234–239.
- Oonk, M. H.; van de Nieuwenhof, H. P.; de Hullu, J. A.; van der Zee, A. G. The Role of Sentinel Node Biopsy in Gynecological Cancer: A Review. *Curr. Opin. Oncol.* **2009**, *21*, 425–432.
- Amersi, F.; Hansen, N. M. The Benefits and Limitations of Sentinel Lymph Node Biopsy. *Curr. Treat. Options Oncol.* **2006**, *7*, 141–151.
- Beri, A.; Janetschek, G. Technology Insight: Radioguided Sentinel Lymph Node Dissection in the Staging of Prostate Cancer. *Nat. Clin. Pract. Urol.* **2006**, *3*, 602–610.
- Winter, A.; Wawroschek, F. Lymphadenectomy in Prostate Cancer. Radio-Guided Lymph Node Mapping: An Adequate Staging Method. *Front. Radiat. Ther. Oncol.* **2008**, *41*, 58–67.
- Tsopelas, C. Particle Size Analysis of (99m)Tc-Labeled and Unlabeled Antimony Trisulfide and Rhenium Sulfide Colloids Intended for Lymphoscintigraphic Application. *J. Nucl. Med.* **2001**, *42*, 460–466.
- Wilhelm, A. J.; Mijnhout, G. S.; Franssen, E. J. Radiopharmaceuticals in Sentinel Lymph-Node Detection—an Overview. *Eur. J. Nucl. Med.* **1999**, *26*, S36–S42.
- Thevarajah, S.; Huston, T. L.; Simmons, R. M. A Comparison of the Adverse Reactions Associated with Isosulfan Blue Versus Methylene Blue Dye in Sentinel Lymph Node Biopsy for Breast Cancer. *Am. J. Surg.* **2005**, *189*, 236–239.
- Simmons, R.; Thevarajah, S.; Brennan, M. B.; Christos, P.; Osborne, M. M. Methylene Blue Dye as an Alternative to Isosulfan Blue Dye for Sentinel Lymph Node Localization. *Ann. Surg. Oncol.* **2003**, *10*, 242–247.
- Cochran, A. J.; Huang, R. R.; Guo, J.; Wen, D. R. Current Practice and Future Directions in Pathology and Laboratory Evaluation of the Sentinel Node. *Ann. Surg. Oncol.* **2001**, *8*, 13S–17S.
- Douglas-Jones, A. G.; Woods, V. Molecular Assessment of Sentinel Lymph Node in Breast Cancer Management. *Histopathology* **2009**, *55*, 107–113.
- Viale, G.; Bosari, S.; Mazzarol, G.; Galimberti, V.; Luini, A.; Veronesi, P.; Paganelli, G.; Bedoni, M.; Orvieto, E. Intraoperative Examination of Axillary Sentinel Lymph Nodes in Breast Carcinoma Patients. *Cancer* **1999**, *85*, 2433–2438.
- Rasmussen, J. C.; Tan, I. C.; Marshall, M. V.; Fife, C. E.; Sevick-Muraca, E. M. Lymphatic Imaging in Humans with near-Infrared Fluorescence. *Curr. Opin. Biotechnol.* **2009**, *20*, 74–82.
- Troyan, S. L.; Kianzad, V.; Gibbs-Strauss, S. L.; Gioux, S.; Matsui, A.; Oketokoun, R.; Ngo, L.; Khamene, A.; Azar, F.; Frangioni, J. V. The Flare Intraoperative near-Infrared Fluorescence Imaging System: A First-in-Human Clinical Trial in Breast Cancer Sentinel Lymph Node Mapping. *Ann. Surg. Oncol.* **2009**, *16*, 2943–2952.
- Song, K. H.; Stein, E. W.; Margenthaler, J. A.; Wang, L. V. Noninvasive Photoacoustic Identification of Sentinel Lymph Nodes Containing Methylene Blue in Vivo in a Rat Model. *J. Biomed. Opt.* **2008**, *13*, 054033.
- Kim, C.; Favazza, C.; Wang, L. V. In Vivo Photoacoustic Tomography of Chemicals: High-Resolution Functional and Molecular Optical Imaging at New Depths. *Chem. Rev.* **2010**, *110*, 2756–2782.
- Hirche, C.; Murawa, D.; Mohr, Z.; Kneif, S.; Hunerbein, M. Icg Fluorescence-Guided Sentinel Node Biopsy for Axillary Nodal Staging in Breast Cancer. *Breast Cancer Res. Treat.* **2010**, *121*, 373–378.
- Jain, R.; Dandekar, P.; Patravale, V. Diagnostic Nanocarriers for Sentinel Lymph Node Imaging. *J. Controlled Release* **2009**, *138*, 90–102.
- Hung, J. C.; Wiseman, G. A.; Wahner, H. W.; Mullan, B. P.; Taggart, T. R.; Dunn, W. L. Filtered Technetium-99m-Sulfur Colloid Evaluated for Lymphoscintigraphy. *J. Nucl. Med.* **1995**, *36*, 1895–1901.
- Phillips, W. T.; Klipper, R.; Goins, B. Use of (99m)Tc-Labeled Liposomes Encapsulating Blue Dye for Identification of the Sentinel Lymph Node. *J. Nucl. Med.* **2001**, *42*, 446–451.
- Tran, T. D.; Caruthers, S. D.; Hughes, M.; Marsh, J. N.; Cyrus, T.; Winter, P. M.; Neubauer, A. M.; Wickline, S. A.; Lanza, G. M. Clinical Applications of Perfluorocarbon Nanoparticles for Molecular Imaging and Targeted Therapeutics. *Int. J. Nanomed.* **2007**, *2*, 515–526.
- Kaneda, M. M.; Caruthers, S.; Lanza, G. M.; Wickline, S. A. Perfluorocarbon Nanoemulsions for Quantitative Molecular Imaging and Targeted Therapeutics. *Ann. Biomed. Eng.* **2009**, *37*, 1922–1933.
- Akers, W. J.; Zhang, Z.; Berezin, M.; Ye, Y.; Agee, A.; Guo, K.; Fuhrhop, R. W.; Wickline, S. A.; Lanza, G. M.; Achilefu, S. Targeting of Av $\beta$ 3-Integrins Expressed on Tumor Tissue and Neovasculature Using Fluorescent Small Molecules and Nanoparticles. *Nanomedicine* **2010**, *5*, 715–726.
- Kim, C.; Song, K. H.; Gao, F.; Wang, L. V. Sentinel Lymph Nodes and Lymphatic Vessels: Noninvasive Dual-Modality in Vivo Mapping by Using Indocyanine Green in Rats—Volumetric Spectroscopic Photoacoustic Imaging and Planar Fluorescence Imaging. *Radiology* **2010**, *255*, 442–450.
- Zhang, Z.; Chen, J.; Ding, L.; Jin, H.; Lovell, J. F.; Corbin, I. R.; Cao, W.; Lo, P. C.; Yang, M.; Tsao, M. S.; et al. Hdl-Mimicking Peptide-Lipid Nanoparticles with Improved Tumor Targeting. *Small* **2010**, *6*, 430–437.
- Lim, Y. T.; Noh, Y. W.; Han, J. H.; Cai, Q. Y.; Yoon, K. H.; Chung, B. H. Biocompatible Polymer-Nanoparticle-Based Bimodal Imaging Contrast Agents for the Labeling and Tracking of Dendritic Cells. *Small* **2008**, *4*, 1640–1645.
- Winter, P. M.; Caruthers, S. D.; Kassner, A.; Harris, T. D.; Chinen, L. K.; Allen, J. S.; Lacy, E. K.; Zhang, H.; Robertson, J. D.; Wickline, S. A.; et al. Molecular Imaging of Angiogenesis in Nascent Vx-2 Rabbit Tumors Using a Novel Alpha(Nu)Beta3-Targeted Nanoparticle and 1.5 T Magnetic Resonance Imaging. *Cancer Res.* **2003**, *63*, 5838–5843.
- Fischer, G. M.; Ehlers, A. P.; Zumbusch, A.; Daltrozzo, E. Near-Infrared Dyes and Fluorophores Based on Diketopyrrolopyrroles. *Angew. Chem., Int. Ed.* **2007**, *46*, 3750–3753.
- Berezin, M. Y.; Akers, W. J.; Guo, K.; Fischer, G. M.; Daltrozzo, E.; Zumbusch, A.; Achilefu, S. Long Fluorescence Lifetime Molecular Probes Based on near Infrared Pyrrolopyrrole Cyanine Fluorophores for in Vivo Imaging. *Biophys. J.* **2009**, *97*, L22–L24.
- Berezin, M. Y.; Lee, H.; Akers, W.; Achilefu, S. Near Infrared Dyes as Lifetime Solvatochromic Probes for Micropolarity

Measurements of Biological Systems. *Biophys. J.* **2007**, *93*, 2892–2899.

31. Almutairi, A.; Akers, W. J.; Berezin, M. Y.; Achilefu, S.; Frechet, J. M. Monitoring the Biodegradation of Dendritic near-Infrared Nanoprobes by in Vivo Fluorescence Imaging. *Mol. Pharmaceutics* **2008**, *5*, 1103–1110.
32. Ye, Y.; Li, W. P.; Anderson, C. J.; Kao, J.; Nikiforovich, G. V.; Achilefu, S. Synthesis and Characterization of a Macrocyclic near-Infrared Optical Scaffold. *J. Am. Chem. Soc.* **2003**, *125*, 7766–7767.
33. Fischer, G. M.; Isomaki-Krondahl, M.; Gottker-Schnetmann, I.; Daltrozzo, E.; Zumbusch, A. Pyrrolopyrrole Cyanine Dyes: A New Class of near-Infrared Dyes and Fluorophores. *Chemistry* **2009**, *15*, 4857–4864.
34. Cho, E. C.; Kim, C.; Zhou, F.; Cobley, C. M.; Song, K. H.; Chen, J. Y.; Li, Z. Y.; Wang, L. H. V.; Xia, Y. N. Measuring the Optical Absorption Cross Sections of Au–Ag Nanocages and Au Nanorods by Photoacoustic Imaging. *J. Phys. Chem. C* **2009**, *113*, 9023–9028.